Supporting Information for

Achieving Large and Anisotropic Spinon Thermal Transport in Textured Quantum Magnets

Shucheng Guo,[1] Xue Bai,[2] Boqun Liang,[3] Thomas Hoke,[1] Ming Liu,[1,3] Rafal E. Dunin-Borkowski,[2] Xi Chen[1,3,*]

1. Department of Electrical and Computer Engineering, University of California, Riverside, California, 92521, USA

2. Ernst Ruska-Centre for Microscopy and Spectroscopy with Electrons, Forschungszentrum Jülich, 52425 Jülich, Germany

3. Materials Science and Engineering program, University of California, Riverside, California, 92521, USA

*Correspondence: xichen@ucr.edu

1. XRD analysis of nano-leaves before and after calcination

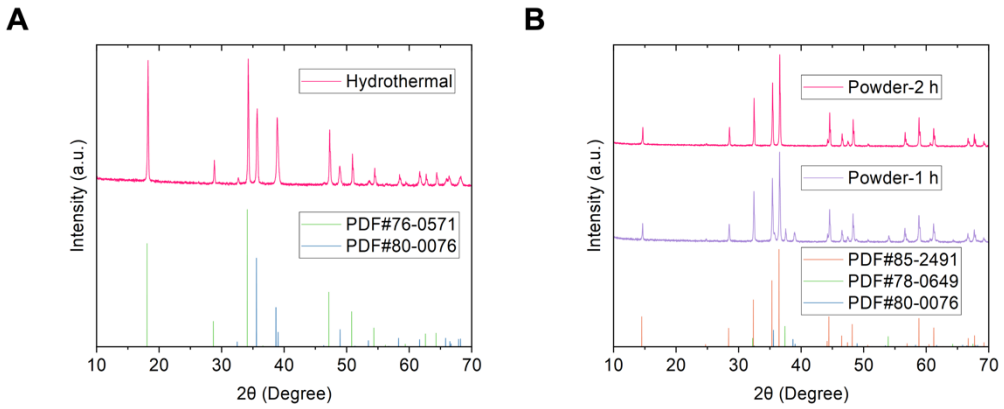

Figure S1: *(A) XRD pattern of the product after hydrothermal treatment. PDF#76-0571 is the standard pattern for* $Ca(OH)_2$*. PDF#80-0076 is the standard pattern for CuO. (B) XRD patterns of the product calcined for 1 hour and 2 hours. PDF#85-2491 is the standard pattern for* Ca_2CuO_3*. PDF#78-0649 is the standard pattern for CaO.*

Figure S1A demonstrates that, after the hydrothermal treatment, the product consists of $Ca(OH)_2$ and CuO. Figure S1B shows that, after 2 hours of calcination at 900˚C, a pure Ca_2CuO_3 phase is formed. When the calcination time is halved to 1 hour, impurities such as CaO and CuO appear. The chemical reactions that take place during the hydrothermal process are therefore:

$$Cu(NO_3)_2 + NaOH \rightarrow Cu(OH)_2 + NaNO_3, (1)$$

$$Cu(OH)_2 \rightarrow CuO + H_2O, (2)$$

$$Ca(NO_3)_2 + NaOH \rightarrow Ca(OH)_2 + NaNO_3. (3)$$

The chemical reactions that take place during the calcination process are:

$$Ca(OH)_2 \rightarrow CaO + H_2O, (4)$$

$$CaO + CuO \rightarrow Ca_2CuO_3. (5)$$

2. XRD analysis of sample prepared by cold pressing

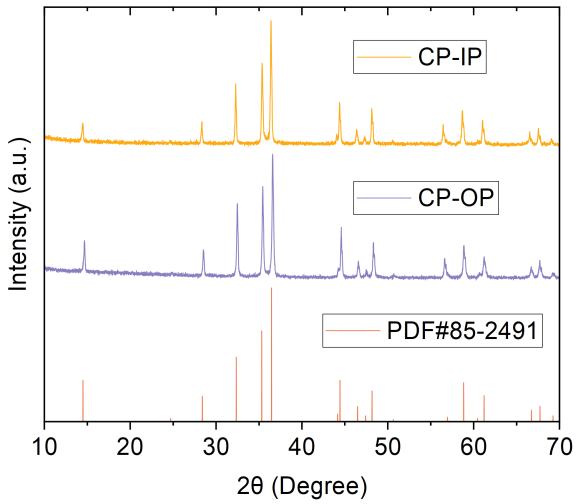

Figure S2: *XRD patterns of sample prepared by cold pressing. PDF#85-2491 is the standard pattern for* Ca_2CuO_3.

Figure S2 shows XRD patterns recorded from the sample prepared by cold pressing (CP), recorded for in-plane (IP) and out-of-plane (OP) directions. The peak intensities of both patterns closely resemble the standard pattern for Ca_2CuO_3 without texture, indicating no significant preferential grain orientation in the CP sample.

3. Analysis of specific heat data

The specific heat (C_p) of electrically insulating Ca_2CuO_3 comprises contributions from lattice vibrations (C_l) and spin excitations (C_s) at low temperatures (T), which is described as:[1]

$$C_p(T) = C_l + C_s = \frac{12xN_A\pi^4k_B}{5} \cdot (\frac{T}{\theta_D})^3 + \frac{2yN_Ak_B^2}{3} \cdot (\frac{T}{J}), \quad (6)$$

where θ_D represents the Debye temperature, k_B is the Boltzmann constant, N_A is the Avogadro constant, J/k_B is the exchange interaction, and x and y denote the number of atoms and the number of magnetic atoms per formula unit, respectively. In order to set $\frac{C_p(T)}{T}$ as the vertical axis and T^2 as the horizontal axis, we perform a linear fit from 5 to 15 K. θ_D and J/k_B can be obtained as follows:

$$\frac{C_p(T)}{T} = \frac{12xN_A\pi^4k_B}{5\cdot\theta_D{}^3} \cdot T^2 + \frac{2yN_Ak_B^2}{3J} = A \cdot T^2 + B, \quad (7)$$

$$\theta_D = (\frac{12xN_A\pi^4k_B}{5\cdot A})^{1/3}, \quad (8)$$

$$J/k_B = \frac{2yN_Ak_B}{3B}, \quad (9)$$

where A is the slope of the fitting curve and B is the intercept with the vertical axis. The obtained value of θ_D is 513 ± 3 K, and J/k_B is 2068 ± 27 K, as shown in the inset to Figure 3A in the main text.

4. Seebeck coefficient measurements

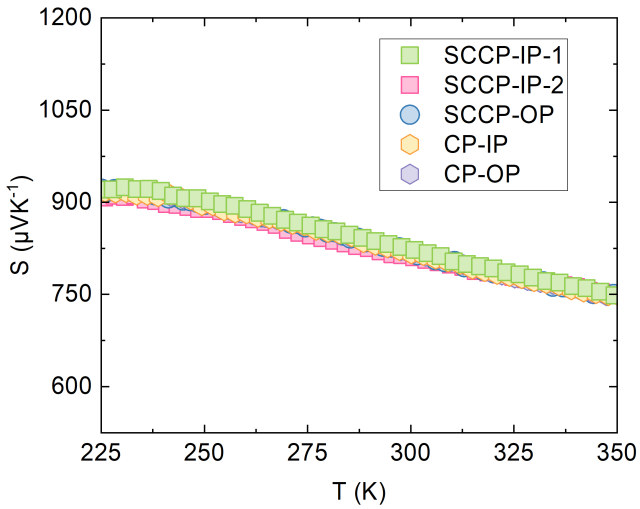

Figure S3: *Seebeck coefficients for the SCCP and CP samples obtained for the IP and OP directions.*

In order to investigate the adverse effects of hole doping, which can attenuate spinon thermal transport by disrupting antiferromagnetic order in cuprates,[2] the Seebeck coefficient (S) was measured. Based on the Pisarenko relation, S correlates inversely with hole concentration.[3] As shown in Figure S3, all of the samples exhibit positive S values of comparable magnitude, implying that their hole concentrations are consistent, and that the effects of hole doping are equivalent across the samples.

5. Thermal conductivity measurement and uncertainty analysis

The samples were cut to standard dimensions of 1 × 1 × 5 mm^3 for measuring their thermal conductivity (κ) using a Quantum Design Physical Property Measurement System (PPMS) between 3 and 350 K. Continuous data recording was performed at a slow rate of T increase of 0.3 K per minute. The software autonomously modified various measurement settings, such as heating power and period.[4] A square wave thermal pulse was applied, and the resulting temperature difference (ΔT) between the hot and cold probes was measured over time. The steady-state temperature difference (ΔT_∞) was established by fitting the data using the formula

$$\Delta T = \Delta T_\infty \times (1 - \frac{\tau_1 \times \exp\left(-\frac{t}{t_1}\right) - \tau_2 \times \exp\left(-\frac{t}{t_2}\right)}{\tau_1 - \tau_2}), \quad (10)$$

where τ_1 and τ_2 represent time constants. After ΔT_∞ has been determined, the thermal conductance (K) can be derived using the following equations:

$$K = P/\Delta T_\infty, \quad (11)$$

$$P = I^2R - P_{rad}, \quad (12)$$

$$P_{rad} = \sigma_T \times (\mathrm{S}/2) \times \varepsilon \times (T_{hot}^4 - T_{cold}^4), \quad (13)$$

where P is the heat flowing through the sample, I is the current flowing into the sample, and R is the resistance of the heater. The Stefan-Boltzmann constant, $\sigma_T = 5.67 \times 10^{-8}$ $Wm^{-2}K^{-4}$, S is the sample's surface area, and ε is its emissivity. T_{hot} and T_{cold} correspond to the temperatures of the hot and cold probes, respectively. Based on these definitions, the value of κ can be derived using the formulae

$$\kappa = K_{sample} \times l/(w \times t), \quad (14)$$

$$K_{sample} = K - K_{shoe}, \quad (15)$$

$$K_{shoe} = aT + bT^2 + cT^3, \quad (16)$$

where K_{sample} is the thermal conductance of the sample, and K_{shoe} is the thermal conductance of the shoe assembly. a, b, and c are constants, while l, w, and t are the distance between the hot and cold probes, the width, and the thickness of the sample, respectively. The accuracy of κ measurement can be affected by various sources of error, such as inaccuracies in the fitting of ΔT, uncertainties in heating power measurement, and errors in calculating radiation losses due to inaccurate estimates of the sample's surface area and emissivity. The surface radiation heat loss for the Ca_2CuO_3 samples has been determined to be below 0.5% of the total heat conduction for

Ca_2CuO_3. It is essential to consider potential errors in K_{shoe} and in the measurements of the sample's dimensions, as well as in l. The total error can be expressed as follows:

$$\sigma(\kappa) = \kappa \times \sqrt{(\frac{R_{\Delta T}}{\Delta T_\infty})^2 + (2\frac{IR\partial I}{P})^2 + (\frac{0.2 \times P_{rad}}{P})^2 + (\frac{0.1 \times T_\infty \times K_{shoe}}{P})^2 + (\frac{\Delta l}{l})^2 + (\frac{\Delta w}{w})^2 + (\frac{\Delta t}{t})^2}, \quad (17)$$

where $R_{\Delta T}$ represents a residual term resulting from the fitting of ΔT *versus* t.

6. Simulation of thermal management using spin chain polycrystals in microelectronic devices

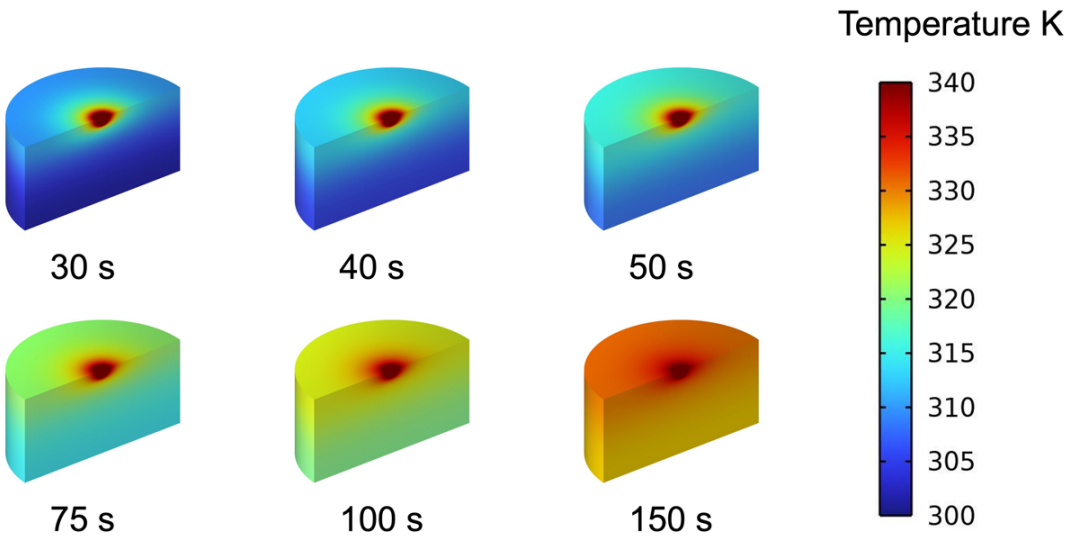

Figure S4: *Simulations of T profile for a highly textured Ca_2CuO_3 polycrystal with a heater on the top surface.*

In order to demonstrate the application of the textured sample for thermal management, the COMSOL Multiphysics heat transfer in solids model was used for finite element analysis (FEA) simulations. Values for the Ca_2CuO_3 cylinder radius of 2.5 mm, height of 2.5 mm, and heat capacity and anisotropic thermal conductivity values were obtained from our measurements. The heat source was set to 340 K and placed on the top surface, and the environment T was set to 293.15 K. A thermal insulation boundary condition was applied to the surfaces of the cylinder. Figure S4 shows that vertical heat transfer is significantly slower than lateral heat transfer due to the large anisotropic thermal conductivity, which is beneficial for directional thermal dissipation in electronic devices.

7. Correction for porosity effect

Based on the Maxwell-Eucken relation, which serves as an effective theoretical framework for calculating κ in two-phase mixtures, especially in porous media,[5] the formula used to eliminate the effect of porosity on κ can be expressed as:[6]

$$\kappa = \kappa_{\text{solid}} \frac{\kappa_{\text{p}}+2\kappa_{\text{solid}}+2\Phi(\kappa_{\text{p}}-\kappa_{\text{solid}})}{\kappa_{\text{p}}+2\kappa_{\text{solid}}-\Phi(\kappa_{\text{p}}-\kappa_{\text{solid}})}, \quad (18)$$

where κ is the detected thermal conductivity, κ_{p} is the thermal conductivity attributable to the pores, Φ denotes the porosity, and κ_{solid} is the value of thermal conductivity when the porosity is 0. Since our experiments are conducted under ultra-high vacuum conditions, thereby eliminating external factors such as air and moisture, the contribution of porous thermal conduction is removed. Therefore, κ_{p} is set to 0, and the simplified Equation. 18 can be written:

$$\kappa_{\text{solid}} = \kappa \frac{2+\Phi}{2-2\Phi}. \quad (19)$$

Furthermore, the Maxwell-Eucken relation, as confirmed by Smith *et al.*, aligns well with experimental data for various oxides when Φ is less than 0.65. It has been applied extensively across numerous material systems with similar porosity levels to our study.[7–12] Since the porosities of samples prepared using the solvent-casting cold pressing (SCCP) and CP methods are 21% and 22%, respectively, *i.e.*, significantly below 65%, the Maxwell-Eucken relation can provide an appropriate correction for the porosity effect in our samples.

8. Extraction process for spinon thermal conductivity of the SCCP sample (Equation. 5 in the main text)

Based on the XRD results from the SCCP sample, the grains are mainly aligned with the b-axis along the IP direction. As the spin chains of Ca_2CuO_3 are aligned along the b-axis and spinon thermal transport occurs exclusively along the 1D spin-chain,[13] the spinon contribution in the OP direction ($\kappa_s^{\mathrm{SCCP-OP}}$) is negligible:

$$\kappa_s^{\mathrm{SCCP-OP}} = 0. \quad (20)$$

Since Ca_2CuO_3 is an insulator,[13] heat can only be carried by lattice vibrations and spin excitations. Consequently, the thermal conductivity measured in the IP ($\kappa^{\mathrm{SCCP-IP}}$) and OP ($\kappa^{\mathrm{SCCP-OP}}$) directions can be expressed as:

$$\kappa^{\mathrm{SCCP-IP}} = \kappa_l^{\mathrm{SCCP-IP}} + \kappa_s^{\mathrm{SCCP-IP}}, \quad (21)$$

$$\kappa^{\mathrm{SCCP-OP}} = \kappa_l^{\mathrm{SCCP-OP}}, \quad (22)$$

where $\kappa_l^{\mathrm{SCCP-IP}}$ and $\kappa_l^{\mathrm{SCCP-OP}}$ are the lattice thermal conductivities in the IP and OP directions, respectively, and $\kappa_s^{\mathrm{SCCP-IP}}$ is the spinon thermal conductivity in the IP direction.

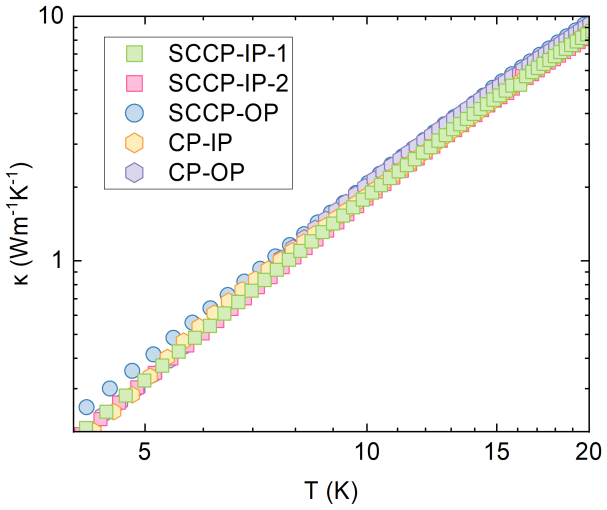

Figure S5: *T-dependence of κ for the SCCP and CP samples measured in the IP and OP directions below 20 K. SCCP-IP-1 and SCCP-IP-2 are oriented perpendicular to each other in the plane orthogonal to the pressing direction.*

At low T, as shown in Figure S5, $\kappa^{\mathrm{SCCP-IP}}$ and $\kappa^{\mathrm{SCCP-OP}}$ exhibit highly consistent T-dependence and values. In this T range, since the spinons are not fully excited, the spinon

contribution to κ is negligible.[14–16] Therefore, $\kappa^{\mathrm{SCCP-IP}}$ is considered to be dominated by $\kappa_l^{\mathrm{SCCP-IP}}$. Moreover, at low T, the crucial factor that restricts phonon thermal transport is phonon-boundary scattering. The consistency between $\kappa^{\mathrm{SCCP-IP}}$ and $\kappa^{\mathrm{SCCP-OP}}$ indicates that, although the SCCP method leads to different morphologies in the IP and OP directions, its impact on phonon thermal transport remains consistent and does not induce strong anisotropic behavior. The lattice contribution is relatively isotropic along the three crystallographic axes in Ca_2CuO_3:[17]

$$\kappa_l^a = \kappa_l^b = \kappa_l^c, \quad (23)$$

where κ_l^a, κ_l^b and κ_l^c are the lattice thermal conductivities of the a-, b- and c-axes, respectively. Therefore, the relationship between $\kappa_l^{\mathrm{SCCP-IP}}$ and $\kappa_l^{\mathrm{SCCP-OP}}$ can be described as:

$$\kappa_l^{\mathrm{SCCP-IP}} = \kappa_l^{\mathrm{SCCP-OP}}. \quad (24)$$

In summary, $\kappa_s^{\mathrm{SCCP-IP}}$ can be determined using the following formula:

$$\kappa_s^{\mathrm{SCCP-IP}} = \kappa^{\mathrm{SCCP-IP}} - \kappa_l^{\mathrm{SCCP-IP}} = \kappa^{\mathrm{SCCP-IP}} - \kappa_l^{\mathrm{SCCP-OP}} = \kappa^{\mathrm{SCCP-IP}} - \kappa^{\mathrm{SCCP-OP}}. \quad (25)$$

9. Extraction process for spinon thermal conductivity of the CP sample

Based on the XRD results from the CP sample, the grains show a random distribution in both the IP and the OP directions. Consequently, spinons are capable of transport in both directions. The thermal conductivity measured from the IP ($\kappa^{\mathrm{CP-IP}}$) and OP ($\kappa^{\mathrm{CP-OP}}$) directions can be expressed as follows:

$$\kappa^{\mathrm{CP-IP}} = \kappa_l^{\mathrm{CP-IP}} + \kappa_s^{\mathrm{CP-IP}}, \quad (26)$$

$$\kappa^{\mathrm{CP-OP}} = \kappa_l^{\mathrm{CP-OP}} + \kappa_s^{\mathrm{CP-OP}}. \quad (27)$$

According to Equation. 23, $\kappa_l^{\mathrm{CP-IP}}$ and $\kappa_l^{\mathrm{CP-OP}}$ have the same values. Since the SCCP and CP samples are prepared from Ca_2CuO_3 nano-leaves that have the same crystal quality, and are synthesized using identical raw materials and annealing conditions, their phonon heat transport properties should be similar. This is confirmed in Figure S5, which shows that $\kappa^{\mathrm{CP-IP}}$ and $\kappa^{\mathrm{CP-OP}}$ almost coincide with $\kappa^{\mathrm{SCCP-IP}}$ and $\kappa^{\mathrm{SCCP-OP}}$ at low T. Combined with the previous discussion on the extraction process of the SCCP sample, $\kappa_l^{\mathrm{CP-IP}}$ and $\kappa_l^{\mathrm{CP-OP}}$ can be described as follows:

$$\kappa_l^{\mathrm{CP-IP}} = \kappa_l^{\mathrm{CP-OP}} = \kappa^{\mathrm{SCCP-OP}}. \quad (28)$$

Therefore, $\kappa_s^{\mathrm{CP-IP}}$ and $\kappa_s^{\mathrm{CP-OP}}$ can be extracted using the relations:

$$\kappa_s^{\mathrm{CP-IP}} = \kappa^{\mathrm{CP-IP}} - \kappa_l^{\mathrm{CP-IP}} = \kappa^{\mathrm{CP-IP}} - \kappa^{\mathrm{SCCP-OP}}, \quad (29)$$

$$\kappa_s^{\mathrm{CP-OP}} = \kappa^{\mathrm{CP-OP}} - \kappa_l^{\mathrm{CP-OP}} = \kappa^{\mathrm{CP-OP}} - \kappa^{\mathrm{SCCP-OP}}. \quad (30)$$

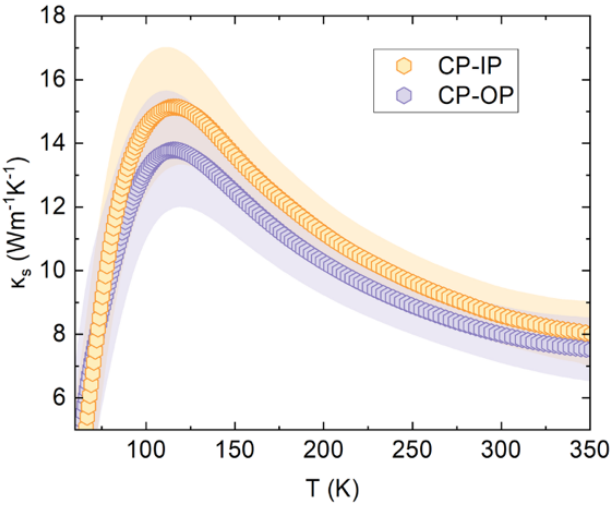

Figure S6: *T-dependence of κ_s for the CP sample for the IP and OP directions.*

Figure S6 illustrates the T-dependence of κ_s for the CP sample in the IP and OP directions, as derived from Equations. 29 and 30. At both high and low T, κ_s in the OP direction is slightly

inferior to that in the IP direction because, although the texture effect of the CP sample is very weak, $F(h0l)$ in the OP direction and $F(020)$ in the IP direction are both greater than 0, confirming that the contribution of the b-axis in the IP direction is stronger than in the OP direction. Thus, spinon thermal transport in the IP direction is slightly larger, leading to the small deviation in Figure S5.

10. Equations for intrinsic spinon thermal conductivity (Equation. 6 in the main text)

In untextured polycrystals, the orientation of each grain is random. As a result, the polycrystalline thermal conductivity (κ^{poly}) can be treated as the average value of the thermal conductivity along the a-, b-, and c-axes, in the form:

$$\kappa^{poly} = \kappa_l^{poly} + \kappa_s^{poly} = \frac{\kappa^a+\kappa^b+\kappa^c}{3}, (31)$$

$$\kappa_l^{poly} = \frac{\kappa_l^a+\kappa_l^b+\kappa_l^c}{3}, (32)$$

where κ^a, κ^b, and κ^c are the thermal conductivities along the a-, b-, and c-axes, respectively, and κ_l^{poly} and κ_s^{poly} are the lattice and spinon thermal conductivities of polycrystals, separately. Furthermore, the spin chains of Ca_2CuO_3 are aligned along the b-axis, and spinon thermal transport occurs exclusively along the 1D spin-chain:[13]

$$\kappa^a = \kappa_l^a, (33)$$

$$\kappa^c = \kappa_l^c, (34)$$

$$\kappa^b = \kappa_l^b + \kappa_s^b, (35)$$

where κ_s^b is the spinon thermal conductivity along the b-axis. Due to its 1D spin-chain structure, the maximum capacity of Ca_2CuO_3 for spinon-based thermal transport can only be realized along the b-axis. This relationship implies that the intrinsic spinon thermal conductivity (κ_s^i) can be described as:

$$\kappa_s^i = \kappa_s^b. (36)$$

Therefore, κ_s^{poly} can be defined as:

$$\kappa_s^{poly} = \kappa^{poly} - \kappa_l^{poly} = \frac{\kappa^a+\kappa^b+\kappa^c}{3} - \frac{\kappa_l^a+\kappa_l^b+\kappa_l^c}{3} = \frac{\kappa_s^b}{3} = \frac{\kappa_s^i}{3}. (37)$$

In this study, both the SCCP and the CP method can induce anisotropy between the IP and OP directions. In order to mitigate the inaccuracies caused by this anisotropy, it is necessary to measure κ in three mutually perpendicular directions: one in the OP direction and two in IP directions. Averaging values obtained in these directions provides a more accurate representation of κ^{poly}.

10.1 For the SCCP sample:

$$\kappa^{poly} = \kappa_l^{poly} + \kappa_s^{poly} = \frac{\kappa^{\mathrm{SCCP-IP-1}}+\kappa^{\mathrm{SCCP-IP-2}}+\kappa^{\mathrm{SCCP-OP}}}{3}, (38)$$

where $\kappa^{\mathrm{SCCP-IP-1}}$ and $\kappa^{\mathrm{SCCP-IP-2}}$ are the thermal conductivity of the SCCP sample measured in the plane orthogonal to the pressing pressure from two mutually perpendicular directions. Based on the previous discussion on the extraction process of the SCCP sample:

$$\kappa_l^{\mathrm{SCCP-IP-1}} = \kappa_l^{\mathrm{SCCP-IP-2}} = \kappa^{\mathrm{SCCP-OP}}. \quad (39)$$

Thus, κ_s^{poly} can be derived as:

$$\kappa_s^{poly} = \kappa^{poly} - \kappa_l^{poly} = \frac{\kappa^{\mathrm{SCCP-IP-1}} + \kappa^{\mathrm{SCCP-IP-2}} + \kappa^{\mathrm{SCCP-OP}}}{3} - \frac{3 \cdot \kappa^{\mathrm{SCCP-OP}}}{3}$$

$$= \frac{\kappa^{\mathrm{SCCP-IP-1}} + \kappa^{\mathrm{SCCP-IP-2}} - 2 \cdot \kappa^{\mathrm{SCCP-OP}}}{3}. \quad (40)$$

In summary, for the SCCP sample, κ_s^i can be obtained using the formula

$$\kappa_s^i = 3 \cdot \kappa_s^{poly} = 3 \cdot \frac{\kappa^{\mathrm{SCCP-IP-1}} + \kappa^{\mathrm{SCCP-IP-2}} - 2 \cdot \kappa^{\mathrm{SCCP-OP}}}{3}$$

$$= \kappa^{\mathrm{SCCP-IP-1}} + \kappa^{\mathrm{SCCP-IP-2}} - 2 \cdot \kappa^{\mathrm{SCCP-OP}}. \quad (41)$$

10.2 For the CP sample:

Because the conventional CP process does not introduce anisotropy in the IP direction, κ remains uniform in two perpendicular directions in the plane orthogonal to the pressing pressure:

$$\kappa^{poly} = \kappa_l^{poly} + \kappa_s^{poly} = \frac{2 \cdot \kappa^{\mathrm{CP-IP}} + \kappa^{\mathrm{CP-OP}}}{3}. \quad (42)$$

Based on the previous discussion of the extraction process of the CP sample:

$$\kappa^{\mathrm{CP-IP}} = \kappa_l^{\mathrm{CP-IP}} + \kappa_s^{\mathrm{CP-IP}} = \kappa^{\mathrm{SCCP-OP}} + \kappa_s^{\mathrm{CP-IP}}, \quad (43)$$

$$\kappa^{\mathrm{CP-OP}} = \kappa_l^{\mathrm{CP-OP}} + \kappa_s^{\mathrm{CP-OP}} = \kappa^{\mathrm{SCCP-OP}} + \kappa_s^{\mathrm{CP-OP}}. \quad (44)$$

Thus, κ_s^{poly} can be derived as:

$$\kappa_s^{poly} = \kappa^{poly} - \kappa_l^{poly} = \frac{2 \cdot \kappa^{\mathrm{CP-IP}} + \kappa^{\mathrm{CP-OP}}}{3} - \frac{3 \cdot \kappa^{\mathrm{SCCP-OP}}}{3} = \frac{2 \cdot \kappa^{\mathrm{CP-IP}} + \kappa^{\mathrm{CP-OP}} - 3 \cdot \kappa^{\mathrm{SCCP-OP}}}{3}. \quad (45)$$

In summary, for the CP sample, κ_s^i can be obtained using the formula

$$\kappa_s^i = 3 \cdot \kappa_s^{poly} = 3 \cdot \frac{2 \cdot \kappa^{\mathrm{CP-IP}} + \kappa^{\mathrm{CP-OP}} - 3 \cdot \kappa^{\mathrm{SCCP-OP}}}{3} = 2 \cdot \kappa^{\mathrm{CP-IP}} + \kappa^{\mathrm{CP-OP}} - 3 \cdot \kappa^{\mathrm{SCCP-OP}}. \quad (46)$$

11. Analysis of defect concentration and energy level splitting using high-field specific heat measurements

To fit the energy level splitting at 5 T ($\Delta_{g,5\,\mathrm{T}}$) and 9 T ($\Delta_{g,9\,\mathrm{T}}$), as well as calculate the defect concentration (n_d), we used only the specific heat values obtained at 5 T ($C_{p,5\,\mathrm{T}}$) and 9 T ($C_{p,9\,\mathrm{T}}$), following Equations 12 and 13 in the main text. The difference in specific heat (ΔC_p,) can be expressed as:[18]

$$\Delta C_p = C_{p,5\,\mathrm{T}} - C_{p,9\,\mathrm{T}} = C_{\mathrm{Sch},5\,\mathrm{T}} - C_{\mathrm{Sch},9\,\mathrm{T}}$$
$$= \frac{\left[\left(\frac{n_d}{2}\right)\cdot R\cdot\left(\frac{\Delta_{g,5\,\mathrm{T}}}{T}\right)^2\cdot e^{\left(\frac{\Delta_{g,5\,\mathrm{T}}}{T}\right)}\right]}{\left[1+e^{\left(\frac{\Delta_{g,5\,\mathrm{T}}}{T}\right)}\right]} - \frac{\left[\left(\frac{n_d}{2}\right)\cdot R\cdot\left(\frac{\Delta_{g,9\,\mathrm{T}}}{T}\right)^2\cdot e^{\left(\frac{\Delta_{g,9\,\mathrm{T}}}{T}\right)}\right]}{\left[1+e^{\left(\frac{\Delta_{g,9\,\mathrm{T}}}{T}\right)}\right]}, \quad (47)$$

where R is the ideal gas constant. Thus, the estimation of Δ_g and n_d is based on the difference observed between high fields (5 T and 9 T) rather than on data below 5 T. The difference between the 5 T and 9 T data is much larger than the measurement uncertainty. The derived values are n_d =0.0057 ± 0.00005 per Cu, Δ_g=1.1 ± 0.02 K at 5 T, and Δ_g=24.6 ± 0.4 K at 9 T.

12. Calculation of spinon mean free path and spinon thermal conductivity

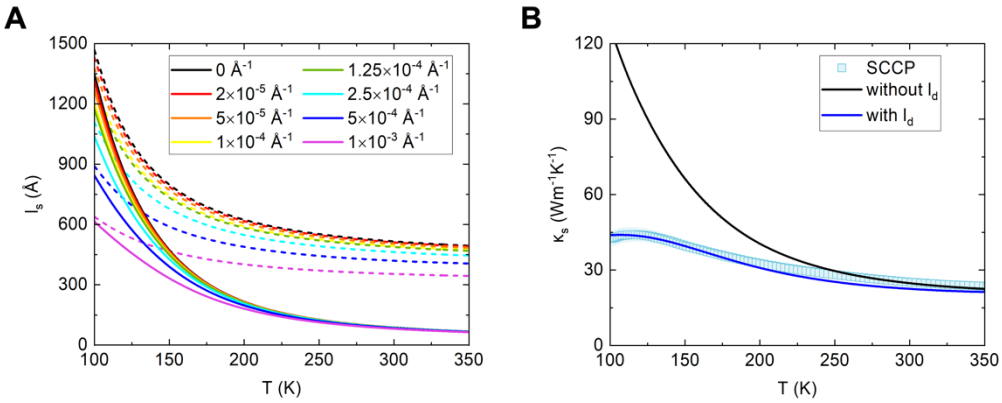

Figure S7: *(A) Calculated T-dependence of the spinon MFP (l_s) under different defect concentrations (n_d). The solid lines represent cases that include the effects of spinon-defect scattering and coupling with low- and high-frequency phonons, while the dashed lines represent cases without coupling to high-frequency phonons. (B) Calculated T-dependence of κ_s with and without considering spinon-defect scattering (l_d). The simulation parameters used are g_{sp-1} =0.24, g_{sp-2} =0.16, and n_d =0.00148 Å^{-1}.*

13. SEM images of the textured La_2CuO_4

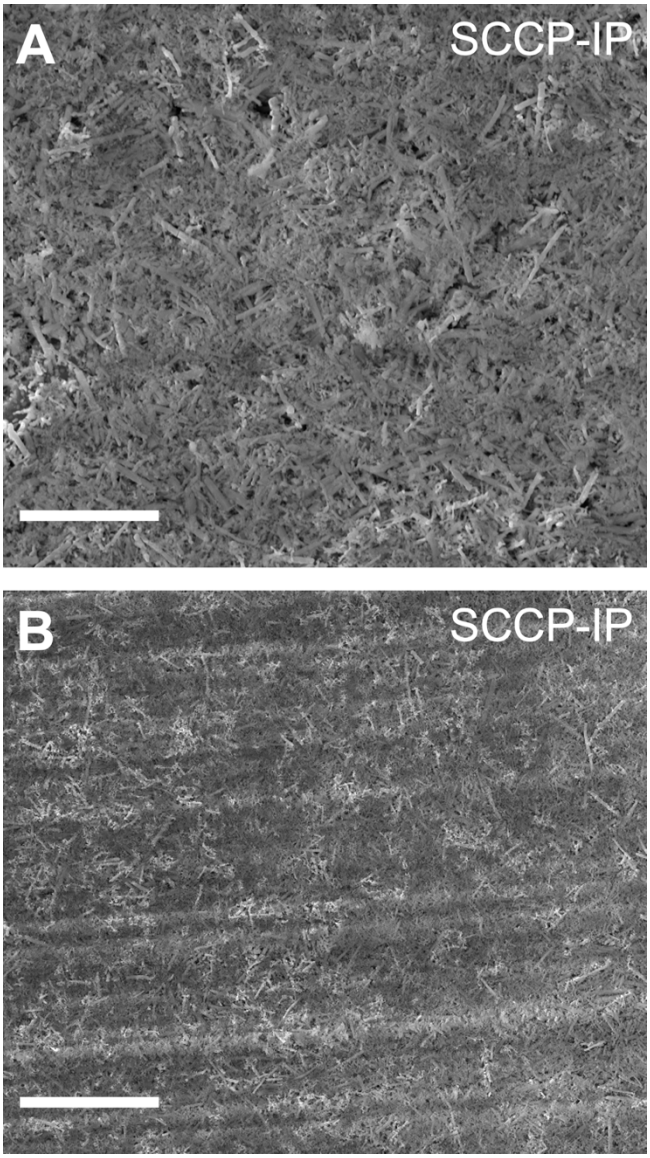

Figure S8: *(A) and (B) SEM images of the textured La_2CuO_4 recorded from a plane oriented along the IP direction. The scale bar in (A) is 10 μm. The scale bar in (B) is 20 μm.*

14. Crystal structure of La_2CuO_4

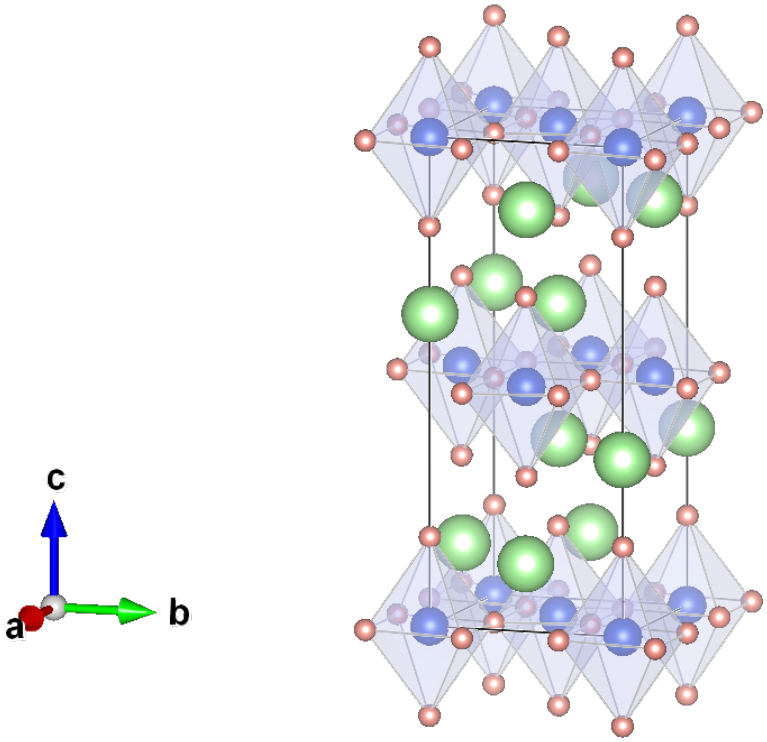

Figure S9: *Crystal structure of La_2CuO_4.*

15. Debye-Callaway model fit for lattice thermal conductivity in textured La_2CuO_4

Hess *et al.*[18] found that below 50 K, the impact of magnons on κ is negligible, with phonon transport taking over as the primary contributor. Consequently, the lower T κ data was fitted using the Debye-Callaway model for 3D phonon transport.[19] The lattice thermal conductivity (κ_l) at higher T was then obtained through extrapolating the fitting results:

$$\kappa_l = \frac{k_\mathrm{B}}{2\pi^2 v_\mathrm{s}} \left(\frac{k_\mathrm{B}T}{\hbar}\right)^3 \int_0^{\theta_\mathrm{D}/T} \frac{x^4 \mathrm{e}^x}{\tau_\mathrm{p}^{-1}(\mathrm{e}^x-1)^2} \mathrm{d}x, \quad (48)$$

where v_s is the sound velocity, $\hbar$ represents the reduced Planck constant, τ_p denotes the phonon relaxation time, and $x = \frac{\hbar\omega}{k_\mathrm{B}T}$. Notably, various scattering processes, such as defect scattering, Umklapp scattering, and boundary scattering, can influence τ_p. Matthiessen's rule allows τ_p to be expressed as a combination of different scattering contributions:

$$\tau_\mathrm{p}^{-1} = \tau_\mathrm{d}^{-1} + \tau_\mathrm{U}^{-1} + \tau_\mathrm{b}^{-1} = A\omega^4 + B\mathrm{e}^{-b/T}T^3\omega^2 + \frac{v_\mathrm{s}}{L}, \quad (49)$$

where A is the fitting parameter for defect scattering, B and b represent fitting parameters for Umklapp scattering, and L is the phonon-boundary scattering mean free path (MFP).

16. Analysis of magnon thermal transport in 2D spin-plane La_2CuO_4

Equation 19 was applied to account for the porosity effect, with Φ_{SCCP} =14% for the textured La_2CuO_4 prepared via the SCCP method. Due to the 2D magnetic structure and high spin-plane symmetry (ab-plane) of La_2CuO_4, κ along the c-axis (κ_c) is governed solely by phonons, while κ within the ab-plane (κ_{ab}) remains isotropic.[20,21] The intrinsic magnon thermal conductivity (κ_m^i) can be defined as:[18,22]

$$\kappa_m^i = \frac{3}{2}\left(\kappa^{poly} - \kappa_l^{poly}\right) = \frac{3}{2}\kappa_m^{poly} = \frac{3}{2}\frac{\left(2\kappa_m^{\mathrm{SCCP-IP}} + \kappa_m^{\mathrm{SCCP-OP}}\right)}{3}, \quad (50)$$

where κ_m^{poly} are the magnon thermal conductivity of polycrystals, and $\kappa_m^{\mathrm{SCCP-IP}}$ and $\kappa_m^{\mathrm{SCCP-OP}}$ represent the magnon thermal conductivity along the IP and OP directions of the SCCP sample, respectively.

Based on a kinetic model for 2D magnon transport, the relationship between the average magnon MFP (l_m) and κ_m^i is given by:[16,18,23]

$$\kappa_m^i = \frac{k_B^3 T^2 l_m}{2\pi\hbar^2 v_0 c}\int_{\frac{\Delta}{k_B T}}^{\infty} x^2\sqrt{x^2 - x_0^2}\,\frac{e^x}{(e^x-1)^2}\,dx, \quad (51)$$

where c =13.2 Å represents the lattice constant of La_2CuO_4 perpendicular to the spin planes, v_0 denotes the spin wave velocity (1.287 × 10^5 ms^{-1}),[24] $\hbar$ is the reduced Planck constant, and Δ is the spin gap of the magnon branch. Here, $x = \frac{\hbar\omega}{k_B T}$ and $x_0 = \frac{\Delta}{k_B T}$. Inelastic neutron scattering study identified two magnon branches with Δ_1/k_B =26 K and Δ_2/k_B =58 K.[25] To ensure complete magnon excitation, Δ_2 was used in calculations.

To quantify the impact of defect scattering (l_d) on magnon thermal transport, l_m can be calculated as:[22,26]

$$l_m^{-1} = l_{xtl}^{-1} + l_b^{-1} + l_d^{-1}, \quad (52)$$

where l_{xtl} is the magnon MFP of the single crystal, l_b denotes the average grain size, and l_d is a frequency-dependent term,[27–30] expressed as $l_d^{-1} = c_d k^3 = c_d \cdot (\frac{k_B}{\hbar v_0})^3 \cdot T^3$.[22] Here, k is wave vector, and c_d is a constant. Based on the single-crystal data reported by Hess et al.,[18] the T-dependent l_m was calculated for various defect concentrations using Equation 52, assuming an infinite grain size (Figure S10A). In addition, l_m for the SCCP sample was fitted, obtaining values of l_b =45 ± 3 × 10^3 Å and c_d =24 ± 2 $Å^2$. These results were subsequently used to calculate the T-dependent κ_m with and without accounting for magnon-defect scattering, applying Equations

51 and 52 (Figure S10B).

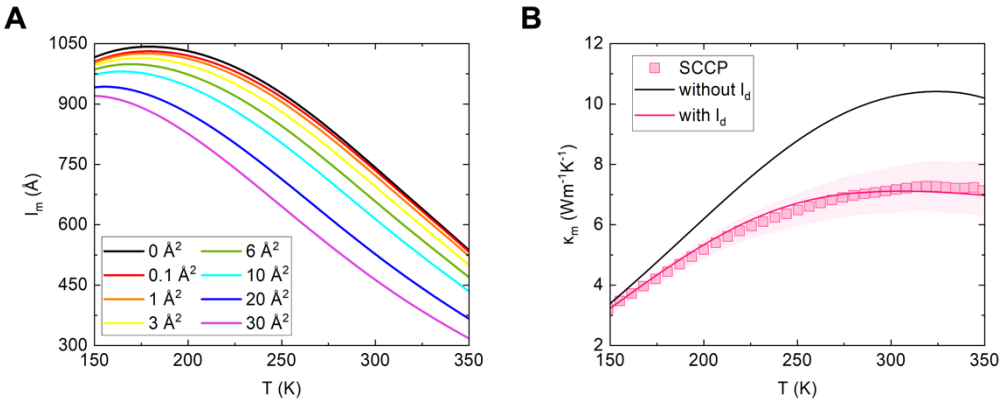

Figure S10: *(A) Calculated T-dependence of the magnon mean free path (l_m) under different defect concentrations (c_d). (B) Calculated T-dependence of κ_m with and without considering magnon-defect scattering (l_d).*

Reference

[1] A. V. Sologubenko, E. Felder, K. Giannò, H. R. Ott, A. Vietkine, A. Revcolevschi, *Phys Rev B* **2000**, 62, R6108.

[2] P. A. Lee, N. Nagaosa, X. G. Wen, *Rev Mod Phys* **2006**, 78, 17.

[3] A. F. Ioffe, *Academic Press*, New York, **1960**.

[4] O. Maldonado, *Cryogenics (Guildf)* **1992**, 32, 908.

[5] F. L. Levy, *Int. J. Refrig* **1981**, 4, 223.

[6] D. S. Smith, A. Alzina, J. Bourret, B. Nait-Ali, F. Pennec, N. Tessier-Doyen, K. Otsu, H. Matsubara, P. Elser, U. T. Gonzenbach, *J Mater Res* **2013**, 28, 2260.

[7] S. Zhao, R. Zhu, Y. Fu, *ACS Appl Mater Interfaces* **2019**, 11, 4588.

[8] A. Nomura et al., *ACS Appl Mater Interfaces* **2018**, 10, 43682.

[9] R. Kroon, J. D. Ryan, D. Kiefer, L. Yu, J. Hynynen, E. Olsson, C. Müller, *Adv Funct Mater* **2017**, 27, 1704183.

[10] S. Rannabauer, G. Söffker, M. Scheunemann, U. Betke, M. Scheffler, *Adv Eng Mater* **2017**, 19, 1700369.

[11] Y. Ying, G. Yang, Y. Tao, Q. Wu, H. Li, *Adv Sci* **2023**, 10, 2204840.

[12] M. B. Østergaard, M. Zhang, X. Shen, R. R. Petersen, J. König, P. D. Lee, Y. Yue, B. Cai, *Acta Mater* **2020**, 189, 85.

[13] K. Foyevtsova, J. T. Krogel, J. Kim, P. R. C. Kent, E. Dagotto, F. A. Reboredo, *Phys Rev X* **2014**, 4, 031003.

[14] A. L. Chernyshev, A. V. Rozhkov, *Phys Rev Lett* **2016**, 116, 017204.

[15] A. V. Sologubenko, K. Giannò, H. R. Ott, A. Vietkine, A. Revcolevschi, *Phys Rev B* **2001**, 64, 054412.

[16] C. Hess, *Phys Rep* **2019**, 811, 1.

[17] X. Chen, J. Carrete, S. Sullivan, A. van Roekeghem, Z. Li, X. Li, J. Zhou, N. Mingo, L. Shi, *Phys Rev Lett* **2019**, 122, 185901.

[18] C. Hess, B. Büchner, U. Ammerahl, L. Colonescu, F. Heidrich-Meisner, W. Brenig, A. Revcolevschi, *Phys Rev Lett* **2003**, 90, 4.

[19] A. V. Sologubenko, K. Giannó, H. R. Ott, U. Ammerahl, A. Revcolevschi, *Phys Rev Lett* **2000**, 84, 2714.

[20] M. Matsukawa, T. Mizukoshi, K. Noto, Y. Shiohara, *Phys Rev B* **1996**, 53, R6034.

[21] D. T. Morelli, J. Heremans, G. Doll, P. J. Picone, H. P. Jenssen, M. S. Dresselhaus, *Phys Rev B* **1989**, 39, 804.

[22] S. Guo, H. Li, X. Bai, Y. Wang, S. Li, R. E. Dunin-Borkowski, J. Zhou, X. Chen, *Cell Rep Phys Sci* **2024**, 5, 101879.

[23] S. R. Boona, J. P. Heremans, *Phys Rev B* **2014**, 90, 064421.

[24] S. M. Hayden, G. Aeppli, R. Osborn, A. D. Taylor, T. G. Perring, S.-W. Cheong, Z. Fisk, *Phys Rev Lett* **1991**, 67, 3622.

[25] B. Keimer, R. J. Birgeneau, A. Cassanho, Y. Endoh, M. Greven, M. A. Kastner, G. Shirane, *Zeitschrift für Physik B Condensed Matter* **1993**, 91, 373.

[26] X. Chen, K. Jarvis, S. Sullivan, Y. Li, J. Zhou, L. Shi, *Phys Rev B* **2017**, 95, 144310.

[27] P. G. Klemens, *Proc. Phys. Soc. A* **1995**, 68, 1113.

[28] L. Lindsay, D. A. Broido, N. Mingo, *Phys Rev B* **2011**, 83, 235428.

[29] P. Carruthers, *Rev Mod Phys* **1961**, 33, 92.

[30] J. Callaway, R. Boyd, *Phys Rev* **1964**, 134, A1655.